

Article

Modulating Surface Morphology Related to Crystallization Speed of Perovskite Grain and Semiconductor Properties of Optical Absorber Layer under Controlled Doping of Potassium Ions for Solar Cells

Tao Ling, Xiaoping Zou *, Jin Cheng, Ying Yang, Haiyan Ren and Dan Chen

Research Center for Sensor Technology, Beijing Key Laboratory for Sensor, Ministry of Education Key Laboratory for Modern Measurement and Control Technology, School of Applied Sciences, Beijing Information Science and Technology University, Jianxiangqiao Campus, Beijing 100101, China; taoling8102@gmail.com (T.L.); chengjin@bistu.edu.cn (J.C.); yang09960@gmail.com (Y.Y.); yanh3100@gmail.com (H.R.); danchen630@gmail.com (D.C.)

* Correspondence: xpzou2005@gmail.com; Tel.: +86-1364-105-6404

Received: 10 July 2018; Accepted: 30 August 2018; Published: 4 September 2018



Abstract: Perovskite thin films with excellent optical semiconductor and crystallization properties and superior surface morphology are normally considered to be vital to perovskite solar cells (PSCs). In this paper, we systematically survey the process of modulating surface morphology and optical semiconductor and crystallization properties of methylammonium lead iodide film by controlling doping of K^+ for PSC prepared in air and propose the mechanism of large K^+ -doped perovskite grain formation related to crystallization speed. The increase in the crystallization speed leads to the production of large grains without localized-solvent-vapor (LSV) pores via moderate doping of K^+ , and the exorbitant crystallization speed induces super large grains with LSV pores via excessive doping of K^+ . Furthermore, the semiconductor properties (absorption band edge wavelength, PL emission peak wavelength, energy band gap) of perovskite film can be significantly tuned by controlled doping of K^+ . The investigation of the detailed process of modulating surface morphology and semiconductor properties of perovskite thin film by controlled doping of K^+ may provide guidance and pave the way for superior component design of absorption materials for cost-efficient PSCs.

Keywords: solar cell; doping of K^+ ; surface morphology; perovskite thin film; crystallization speed; semiconductor properties

1. Introduction

Recently, perovskite solar cells (PSCs) were considered, by the public, as the most promising alternative photovoltaic devices as a result of their simple process and high efficiency [1–5]. Undoubtedly, perovskite thin film with superior surface morphology (such as better flatness, low defect density, and large and dense crystal grains) [6–9] and excellent semiconductor properties (such as suitable exciton binding energy, long carrier lifetime, and appropriate band gap) [6,10–12], is normally considered to be vital for PSCs. In order to optimize some semiconductor properties of perovskite materials (such as the interface energy barrier, contact resistance, and carrier diffusion length), some intended doping has been used in absorbing materials based on photovoltaic devices [6,13–22].

Previously, there were some published reports, which showed that Cs- and Rb-doped PSCs had better stability and higher power conversion efficiency (PCE) than pure PSCs [3,15–17]. In addition,

some research groups reported that K- and Na-doped perovskites also had better PCE [5,18–22]. Huang et al. confirmed that Na⁺ can decrease defect density in perovskite absorbers [22]. In our research group, Bai and Yang demonstrated that Rb⁺ [11] and Na⁺ [12] can change carrier concentration and mobility, respectively, in perovskite absorbers.

Specially, Tang et al. found that K⁺ can eliminate the barrier and reduce the defect of perovskite [5,23]. In addition, Zhao et al. reported the modified surface work function, improved crystallinity, and prolonged carrier lifetime in perovskite film via doping of K⁺ [20]. Yao et al. demonstrated that K⁺ prefers to occupy the interstitial site in the lattice of perovskite [24]. Kubicki et al. reported that there are unreacted KI and KPbI₃ in K-doped perovskite thin film [25]. Abdi-Jalebi et al. reported the substantial mitigation of both non-radiative losses in perovskite films and interfaces with passivating potassium halide layers [26]. Although there are a few reports on doping of K⁺ in perovskite materials [5,18,20,23–27], a detailed report on the mechanism of large perovskite grain formation related to crystallization speed (CS) in K⁺-doped perovskite thin films has not been seen up to now, which is also important for the research of K⁺-doped perovskite thin film for solar cells.

Although certified PCE > 20% was obtained via tuning of the process and composition of perovskite thin film of PSCs [28,29], these devices have been obtained by various processes, which contains a necessary step of forming counter electrode (CE) by thermal evaporation of metals. Apparently, the costs of these metallic CEs are relatively high. To reduce the costs of PSCs, some researchers have developed carbon CEs [30–32]. Yang et al. prepared a 2.6% efficient original perovskite solar cell with a candle soot carbon/FTO CE [30]. In our research group, previously, a spongy carbon/FTO composite structure was adopted as a CE and the corresponding cell achieved 4.24% PCE [33], and recently, a PSC with this kind of composite CE was prepared via sequential deposition route and achieved 10.7% PCE [34].

This time, we systematically survey the process of modulating surface morphology and optical semiconductor and crystallization properties of methylammonium lead iodide (MAPbI₃) thin film via controlled doping of K⁺ for PSC prepared in air. In addition, we propose the mechanism of large perovskite grain formation on CS and doping concentration of K⁺. The increase in the CS leads to the production of large grains without localized-solvent-vapor (LSV) pores via moderate doping of K⁺ and the exorbitant crystallization speed induces super large grains with LSV pores via excessive doping of K⁺. Furthermore, the optical semiconductor and crystallization properties of perovskite film prepared in air could be significantly tuned by doping of K⁺. We also observed the transition from blue shift to red shift of the absorption band edge wavelength with the increase in the amount of doping of K⁺, which is consistent with the shift of the PL emission peak wavelength. Although this transition did not exist in the results of most research groups [5,20,23], it has occurred [18]. The PSC was prepared via a one-step solvent process under ambient conditions and also resulted in a promising 8.14% PCE on the area of 0.2 cm².

2. Materials and Methods

2.1. Materials

Fluorine-doped SnO₂ (FTO) substrates were purchased from Dalian HeptaChroma Solar Technology Development Corp (Dalian, China). Dimethyl sulfoxide (DMSO) and N,N-dimethylformamide (DMF) were obtained from Sa'en Chemical Technology Corp (Shanghai, China). 18NR-T TiO₂ paste (M-TiO₂), isopropyl alcohol (IPA), PbI₂, chlorobenzene, and acidic titanium dioxide solution (C-TiO₂) were obtained from Shanghai MaterWin New Materials Corp (Shanghai, China). Spiro-OMeTAD solution, Methylammonium iodide (MAI), and KI were obtained from Xi'an Polymer Light Technology Corp (Xi'an, China).

2.2. Device Fabrication

The cleaning method of FTO and deposition processes of C-TiO₂ layer, M-TiO₂ layer and Spiro-OMeTAD layer are the same as those previously [34]. The preparation method of the perovskite thin film deposit and counter electrode will be introduced next. MAPbI₃ solution was prepared by mixing 1.2 M CH₃NH₃I and 1.3 M PbI₂ in a mixed solvent (DMF:DMSO = 4:1). Then, 0.6, 0.9 and 1.2 M KI solution was prepared by dissolving a corresponding amount of KI solid in 200 µL mixed solvent (DMF:DMSO = 4:1). These solutions were added to 1 mL prepared MAPbI₃ solution. These precursor solutions were spin coated on the M-TiO₂/C-TiO₂/FTO substrate through two periods at 1000 rpm for 10 and 3000 rpm for 30 s. During the second period, 20 µL of chlorobenzene was dropped at 15 s prior to the end of the period. Then, a thermal annealing of 100 °C for 15 min was processed to yield perovskite films. Finally, the FTO substrates were used to collect the soot of a burning candle as spongy carbon CEs and these spongy carbon films on FTO glasses were then pressed on the as-prepared uncompleted devices.

2.3. Characterization

The details of scanning electron microscopy (SEM) with energy spectrum analysis, X-ray diffraction (XRD) are the same as those used before [34]; however, the absorption spectra of perovskite films with different doping concentrations of K⁺ were analyzed by an ultraviolet visible (U-V) absorption spectrometer (Avantes, Apeldoorn, The Netherlands) and the PL was examined by a LabRAW HR800 PL testing system (HORIBA Jobin Yvon, Paris, France).

3. Results and Discussion

The K⁺ doping contents of 1.2 mL perovskite precursor solutions with the addition of 200 µL KI solutions of 0 M, 0.6 M, 0.9 M and 1.2 M were named 0M, 0.6M, 0.9M and 1.2M, respectively. The MAPbI₃ films with 0 M, 0.6 M, 0.9 M and 1.2 M were named MAPbI₃+0M, MAPbI₃+0.6M, MAPbI₃+0.9M and MAPbI₃+1.2M, respectively. Surface and cross-sectional SEM images for perovskite absorber layers with 0 M, 0.6 M, 0.9 M and 1.2 M are presented in Figure 1, where we can see clearly the process of modulating surface morphology of the perovskite thin film via controlled doping of K⁺. In Figure 1e–h, we can see clearly the perovskite layer, M-/C-TiO₂ (Mesoporous-TiO₂ and Compact-TiO₂) layer and FTO layer from the top to the bottom. Although the surface of MAPbI₃+0M (presented in Figure 1a) is relatively flat, there are many pores (presented in yellow circle, Figure 1e) in the interface between MAPbI₃+0M and M-/C-TiO₂. In addition, the sizes of grains are relatively smaller and there are more vertical grain boundaries in MAPbI₃+0M (presented in the white circle, Figure 1e). Relative to MAPbI₃+0M, the surface of MAPbI₃+0.6M (presented in Figure 1b) is rough, but pores are not present in the interface between perovskite layer and M-/C-TiO₂, which means the doping of K⁺ can passivate the interface between MAPbI₃+0M and M-/C-TiO₂. Furthermore, the sizes of grains are bigger, and there are fewer transverse grain boundaries (presented in Figure 1b). As for MAPbI₃+0.9M (Figure 1c,g), the surface has better flatness and grains are larger than for MAPbI₃+0.6M, so that the transverse grain boundaries are greatly reduced and vertical grain boundaries are almost gone, which lead to a great improvement in its efficiency. From Figure 1d, we can find a super large grain (>4 µm in the longest direction), but there are LSV pores (presented in blue circle), boundary gaps (presented in yellow circle) and unidentified square protrusions (presented in red circle) on the surface of MAPbI₃+1.2M. It is more important to note that there are also LSV pores (presented in blue circle) inside MAPbI₃+1.2M according to Figure 1h, which greatly reduces the efficiency of the device. These LSV pores are caused by the inefficient discharge of the solvent from the interior of crystallizing perovskite due to the exorbitant perovskite CS. Through the comparison of these cross-sectional SEM images (Figure 1e–h), we can find that MAPbI₃+1.2M becomes very thick (~900 nm). Furthermore, the perovskite grain sizes increases (~500 nm, ~700 nm, ~2 µm and ~4 µm, on average, corresponding MAPbI₃+0M, MAPbI₃+0.6M, MAPbI₃+0.9M and MAPbI₃+1.2M, respectively) with the increase in the

doping concentration of K^+ according to the comparison of these surface SEM images (Figure 1a–d). The perovskite grain sizes increase with the increase in the doping concentration of K^+ so that the number of grain boundaries of perovskite films decreases. In addition, the decomposition of perovskite films begins at the boundaries of perovskite grains, so the stability of devices increases with the increase in the doping concentration of K^+ .

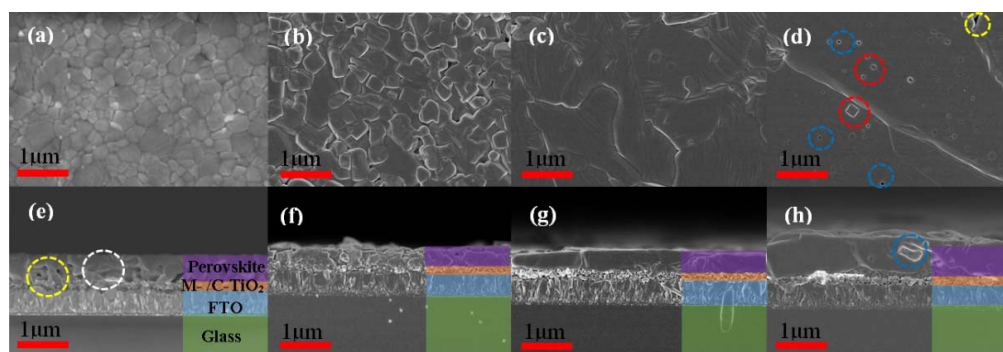


Figure 1. Surface and cross-sectional SEM images for (a,e) $MAPbI_3+0M$; (b,f) $MAPbI_3+0.6M$; (c,g) $MAPbI_3+0.9M$; (d,h) $MAPbI_3+1.2M$.

According to these experimental results, we propose the following mechanism (presented in Figure 2) of large K^+ -doped perovskite grain formation related to CS. In Figure 2, the red arrow represents the solvent evaporation (SE) direction and the small black spot represents seed crystal, which is the root of the formation of perovskite grain. We assume that the distributions of seed crystals in all samples are the same during the initial stage. Lower CS (corresponding to the absence of doping) leads to relatively more spaces to form seed crystals in the perovskite solution due to smaller crystallizing grains during the intermediate stage, which results in smaller grains and more grain boundaries during the final stage eventually. Suitable CS causes larger crystallizing perovskite grains and less spaces for the formations of new seed crystals during the intermediate stage via moderate doping of K^+ , and finally, the large grains without LSV pores formed. However, excessive doping can cause exorbitant CS and leads to super large crystallizing grain during the intermediate stage, so that there are almost no spaces to form new seed crystals and the solvent can only be evaporated upwards for filling of the whole space by the transverse crystallizing grains, which cause the solvent to not effectively discharge from the interior of crystallizing perovskite; as a result, LSV pores are formed inside the perovskite thin films and on its surface during the final stage. The crystallization already starts when the seed crystal form and it may be during solvent evaporation when the spin-coating or the process of chlorobenzene addition or thermal annealing occur. Irrespective, the schematic mechanism in Figure 2 is adaptive. In addition, it is worth emphasizing that new seed crystals may form at all times, and once the seed crystals form, the process described by the schematic mechanism takes place.

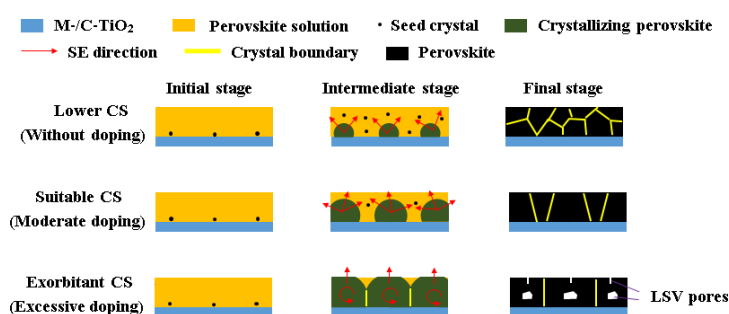


Figure 2. Schematic illustration for the mechanism of large K^+ -doped perovskite grain formation related to crystallization speed.

To back up this theory that the CS of perovskite increases with the increase in the K doping amount, we analyze the results of previous research. Uz Zaman et al. prepared K-doped perovskite thin films on FTO substrates by spin coating [35], which are hydrophobic substrates, and the perovskite solution films must shrink after spin coating, unavoidably so that the final perovskite films cannot completely cover the substrates. We can find that the coverage area of perovskite thin films increases with the increase of the K doping amount according to their SEM results [35]. The coverage rate of perovskite thin film on substrate is mainly determined by the strength of the solution thin film shrinkage and the CS of perovskite, illustrated in Figure 3. In Figure 3, the red arrow marks the shrinkage direction of the perovskite solution thin film and the small black dot represents the perovskite seed crystal. In the process of perovskite solution film shrinking, perovskite crystals are also growing in areas with perovskite precursor solution, so that stronger shrinkage strength leads to a smaller coverage rate and faster crystallization speed leads to a greater coverage rate. The shrinkage strength of the perovskite solution film is mainly determined by the solvent and substrate; however, the solvents of the perovskite precursor solutions with different K content and substrates are exactly the same, so the shrinkage strengths of perovskite solution films are almost the same. Thus, the conclusion can be reached that different crystallization speeds lead to different perovskite film coverage rates, and the crystallization speed of perovskite increases with the increase in the K doping amount. The crystallization speed of perovskite we expect can make the grain grow to a large state without localized-solvent-vapor (LSV) pores or with small number of LSV pores of which the inducing efficiency attenuation is less than the benefit from the increase in grain size. According to SEM diagrams and JV curves, the expected speed is between the speed corresponding 0.9 M and the speed corresponding 1.2 M because $\text{MAPbI}_3+0.9\text{M}$ does not have LSV pores and $\text{MAPbI}_3+0.9\text{M}$ has LSV pores, which induce efficiency attenuation. Exorbitant crystallization speed can make the grain grow to a large state with more LSV pores of which the inducing efficiency attenuation is higher than the benefit from the increase in grain size, so the speed corresponding to 1.2 M is an exorbitant crystallization speed.

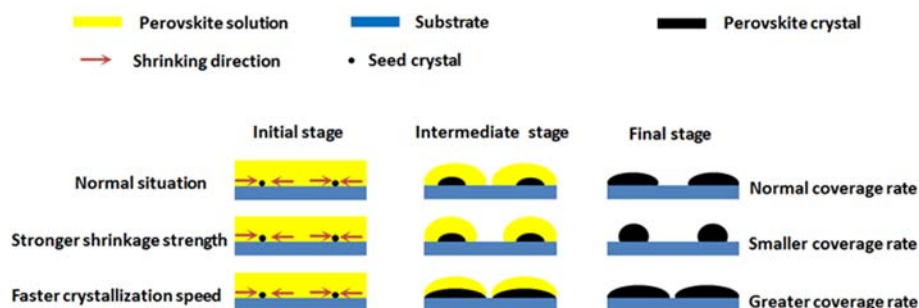


Figure 3. Schematic illustration for the formation of different coverage rates on the hydrophobic substrate due to different solution thin film shrinkage strength and the crystallization speed of perovskite.

Figure 4a shows XRD pattern of perovskite thin films with different doping concentration of K^+ and we can find that the peak position of perovskite crystal has not been transferred, which means there is no change in the type of perovskite crystal structure via different concentration doping of K^+ [36]. In addition, the perovskite film exhibits pure tetragonal phase according to Figure 4a, which indicates that the K^+ enters into the perovskite lattice successfully [20]. From Figure 4b, we noticed that the perovskite crystallization is improved with the increase in the K doping amount, which indicates a longer carrier lifetime [20]. Compared to MAPbI_3+0M , almost all other (040) peaks shift to lower degree in Figure 4c, which means K^+ mainly occupied interstitial sites in lattices [20].

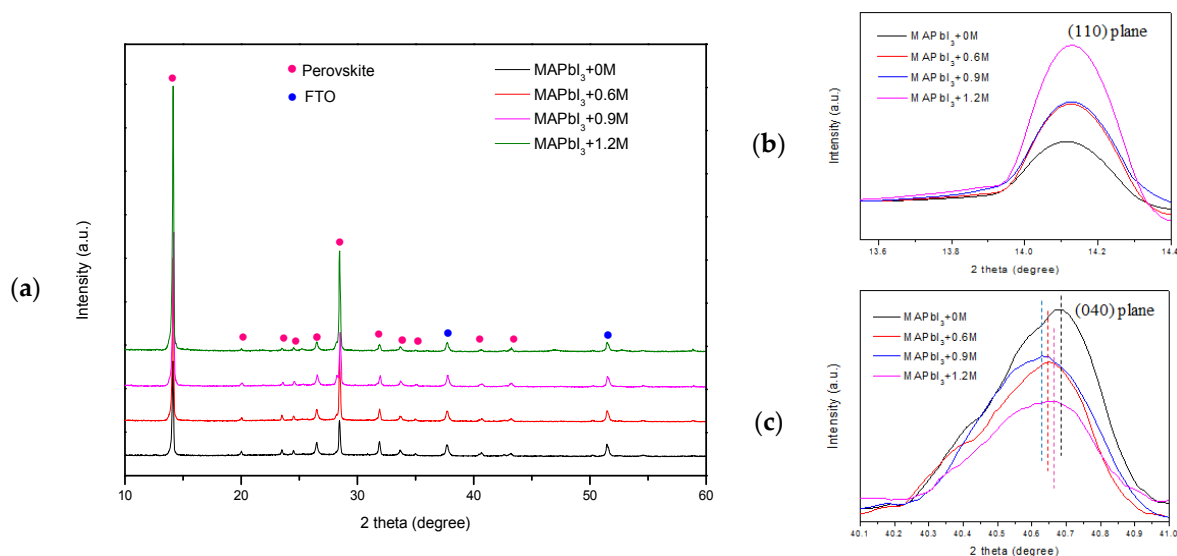


Figure 4. XRD patterns of perovskite films with 0 M, 0.6 M, 0.9 M and 1.2 M: (a) whole patterns; (b) enlargement of (110) crystal plane; (c) enlargement of (040) plane.

The Energy dispersive X-ray Spectroscopy (EDX) of K-doped perovskite crystallite films and the specific values of quantifying doping levels are presented in Figure 5 and Table 1, respectively. In the EDXs (Figure 5a–d), we can see that the peaks of K elements (presented in blue circle) increase with the increase in the doping concentration, which is consistent with the values in Table 1. The excess iodine coming from the KI solution can also affect the perovskite film performance, which is carried out by Equation (1) [37] and Equation (2) [37,38].



However, I_3^{-} can effectively decrease the concentration of defects in organic-inorganic lead halide perovskite films [38].

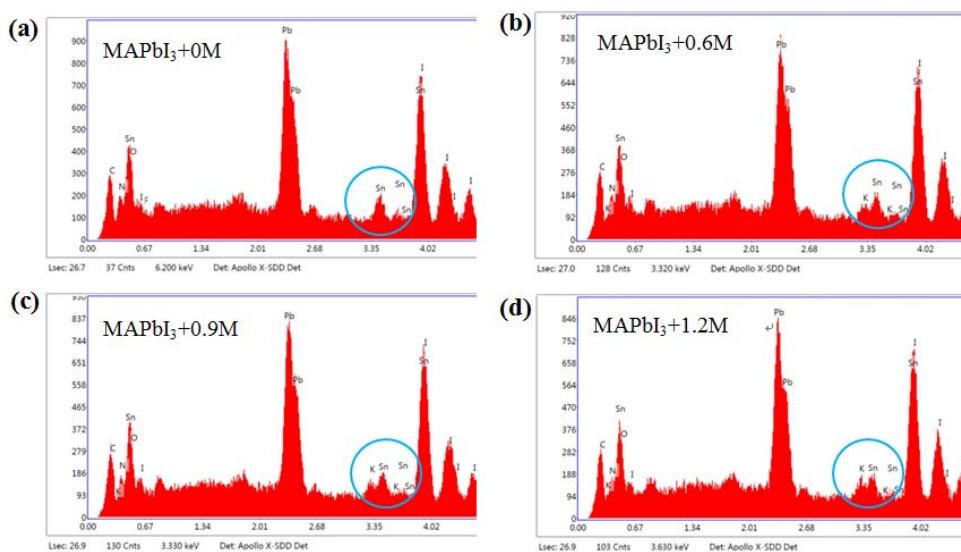
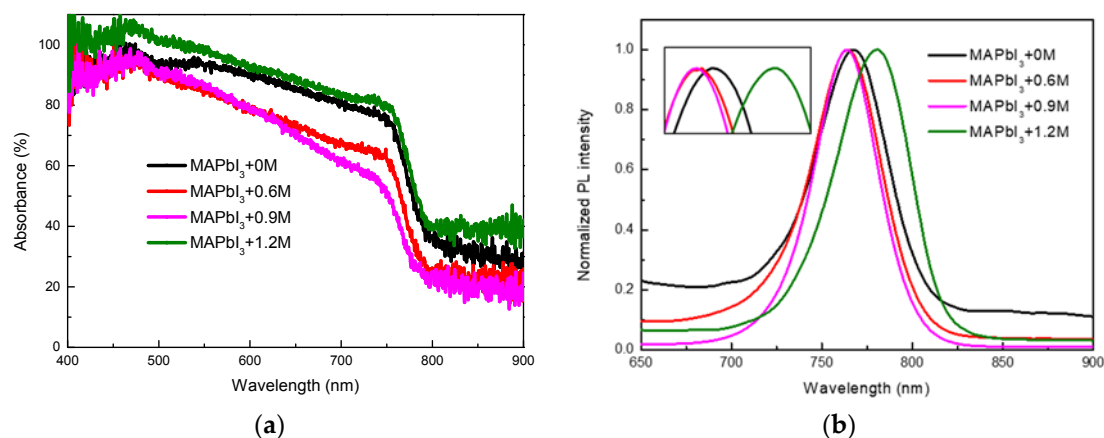


Figure 5. The Energy dispersive X-ray Spectroscopy (EDX) of perovskite films with 0 M, 0.6 M, 0.9 M and 1.2 M.

Table 1. EDX identified element percentages (weight %) in the perovskite films with 0 M, 0.6 M, 0.9 M and 1.2 M.

Sample	K K	C K	N K	O K	Pb M	Sn L	I L
MAPbI ₃ +0M	0	5.10	2.35	0.80	23.49	5.84	62.42
MAPbI ₃ +0.6M	1.44	4.58	2.18	0.49	21.77	5.40	64.14
MAPbI ₃ +0.9M	1.50	4.59	1.73	0.38	22.21	5.67	63.92
MAPbI ₃ +1.2M	1.80	4.50	2.07	0.55	21.71	5.26	64.11

Figure 6a,b show the absorbance spectra and PL spectra of perovskite thin films with 0 M, 0.6 M, 0.9 M and 1.2 M, respectively. There are blue shifts of the absorption band edge wavelength and PL emission peak wavelength of MAPbI₃+0.6M and MAPbI₃+0.9M, and the red shift the absorption band edge wavelength and PL emission peak wavelength of MAPbI₃+1.2M has taken place, compared to reference MAPbI₃+0M, indicating that the energy band gap increases first and then decreases with the increase in the doping concentration of K⁺ [5].

**Figure 6.** (a) Absorbance spectra and (b) PL spectra of perovskite thin films with 0 M, 0.6 M, 0.9 M and 1.2 M.

Schematic illustration for the process of modulating surface morphology related to CS and optical semiconductor properties of perovskite thin films via controlled doping of K⁺ is shown in Figure 7. It gives a very detailed description of the process of modulating surface morphology (including grain size, surface flatness, transverse and vertical grain boundary quantity, internal LSV pores, surface LSV pores, pores in the interface between perovskite layer and M-/C-TiO₂, thickness of perovskite thin film, boundary gap) and optical semiconductor properties (absorption band edge wavelength, PL emission peak wavelength, energy band gap) of perovskite thin film via controlled doping of K⁺ prepared in air. It is worth emphasizing that the mechanism of large K⁺-doped perovskite grain formation is related to CS. The doping of K⁺ leads to an increase in CS of perovskite grains during the intermediate stage, and results the formation of large perovskite grains during the final stage. However, excessive doping of K leads to a rapid perovskite crystallization speed that induces super large crystallizing grains and causes the solvent to not effectively discharge from crystallizing perovskite during the intermediate stage; as a result, LSV pores are formed inside the perovskite thin films and on its surface during the final stage.

The structure of the device is shown in Figure 8a. Figure 8b shows the J-V curves from RS for the devices with different doping concentrations of K⁺, measured under simulated sunlight (AM 1.5 G), and the detail photovoltaic parameters of PSCs is shown in the Table 2. V_{oc} has increased significantly via controlling doping of K⁺, as a result of elimination of pores in the interface between the perovskite layer and M-/C-TiO₂ layer. Due to larger grains in the MAPbI₃+0.9M and MAPbI₃+1.2M,

the corresponding devices obtain higher J_{sc} . Although the absorption spectrum of $MAPbI_3+0.9M$ is relatively low compared to other perovskite films, its device yielded the best performance (especially the V_{oc} and J_{sc}) due to prolonged carrier lifetime, improved surface morphology and crystallinity, which means the photovoltaic properties of the devices are improved via appropriate doping of K^+ . A promising efficiency of 8.14% was achieved for the 0.9 M K^+ -doped device with the carbon/FTO CE, and these simple and low-cost preparation techniques of high-class perovskite thin films and carbon/FTO CE under ambient conditions are beneficial for promoting commercialization.

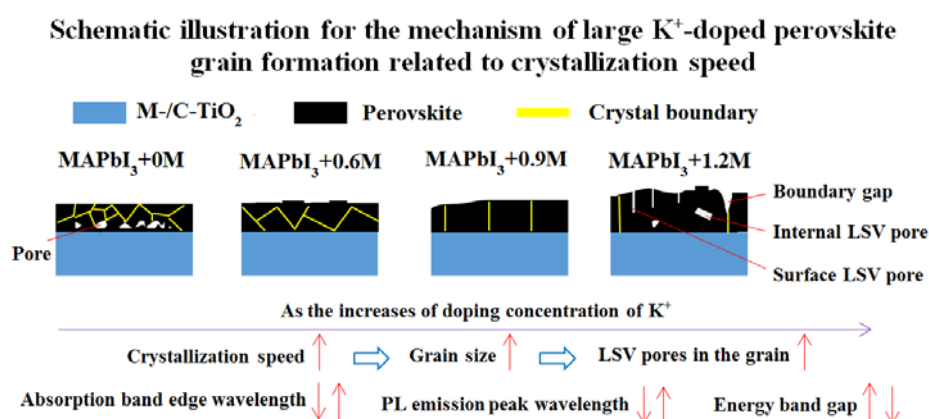


Figure 7. Schematic illustration for the process of modulating surface morphology related to CS and optical semiconductor properties of perovskite thin film via controlled doping of K^+ prepared in air.

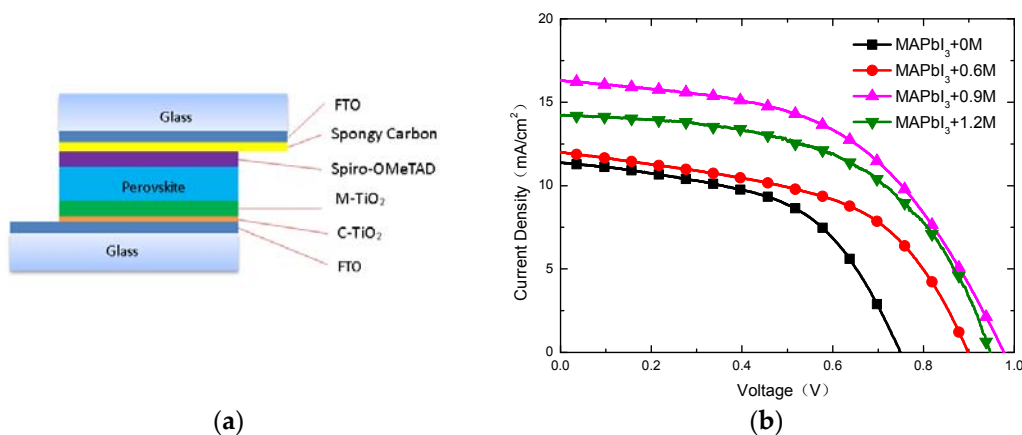


Figure 8. (a) Schematic illustration for the structure of devices; (b) Light current-voltage (J-V) curves from reverse scan (RS) for the devices with 0 M, 0.6 M, 0.9 M and 1.2 M under RS.

Table 2. Photovoltaic parameters of PSCs with 0 M, 0.6 M, 0.9 M and 1.2 M under RS.

DC ^a	J_{sc} ^b (mA/cm^2)	V_{oc} ^c (v)	FF ^d	PCE (%)
0 M	11.37	0.75	0.52	4.43
0.6 M	12.01	0.90	0.52	5.62
0.9 M	16.33	0.98	0.51	8.14
1.2 M	14.20	0.95	0.55	7.42

^a DC: Doping concentration of K^+ ; ^b J_{sc} : Short-circuit photocurrent density; ^c V_{oc} : Open-circuit voltage; ^d FF: Fill factor.

4. Conclusions

The LSV-pore-free perovskite grains became significantly larger via moderate doping of K^+ . The mechanism of large K^+ -doped perovskite grain formation is related to CS and the theory that the CS of perovskite increases with the increase of K doping amount was suggested and preliminarily confirmed. The detailed description of the process of modulating surface morphology (including grain size, surface flatness, transverse and vertical grain boundary quantity, internal LSV pores, surface LSV pores, pores in the interface between $MAPbI_3+0M$ and $M-/C-TiO_2$, thickness of perovskite thin film, boundary gap) and optical semiconductor properties (absorption band edge wavelength, PL emission peak wavelength, energy band gap) of perovskite thin film via controlled doping of K^+ prepared in air was presented. A promising efficiency of 8.14% in a size of 0.2 cm^2 was achieved for the device with inexpensive carbon/FTO CE under one sun illumination. Obviously, mass production of cost-efficient K^+ -doped PSCs, with spongy carbon/FTO CEs, under ambient atmosphere, is possible.

Author Contributions: T.L. wrote the paper. Y.Y. designed the experiments. T.L. and J.C. analyzed the data. D.C. prepared the samples. T.L. and H.R. performed all the measurements. X.Z. supervised the project. All authors commented and approved the paper.

Funding: This research was funded by the Project of the Natural Science Foundation of China (61875186), the Project of the Natural Science Foundation of Beijing (Z160002), the Opened Fund of the State Key Laboratory on Integrated Optoelectronics (IOSKL2016KF19) and the Beijing Key Laboratory for Sensors of BISTU (KF20181077203).

Conflicts of Interest: The authors declare no conflict of interest.

References

1. Park, N.-G. Organometal perovskite light absorbers toward a 20% efficiency low-cost solid-state mesoscopic solar cell. *J. Phys. Chem. Lett.* **2013**, *4*, 2423–2429. [[CrossRef](#)]
2. Yang, W.S.; Noh, J.H.; Jeon, J.N.; Kim, Y.C.; Ryu, S.C.; Seo, S.J.; Seok, S.I. High-performance photovoltaic perovskite layers fabricated through intramolecular exchange. *Science* **2015**, *348*, 1234–1237. [[CrossRef](#)] [[PubMed](#)]
3. Saliba, M.; Matsui, T.; Domanski, K.; Seo, J.-Y.; Ummadisingu, A.; Zakeeruddin, S.M.; Correa-Baena, J.-P.; Tress, W.R.; Abate, A.; Hagfeldt, A.; et al. Incorporation of rubidium cations into perovskite solar cells improves photovoltaic performance. *Science* **2016**, *354*, 206–209. [[CrossRef](#)] [[PubMed](#)]
4. Shin, S.S.; Yeom, E.J.; Yang, W.S.; Hur, S.; Kim, M.G.; Im, J.; Seo, J. Colloidally prepared La-doped $BaSnO_3$ electrodes for efficient, photostable perovskite solar cells. *Science* **2017**, *356*, 167–171. [[CrossRef](#)] [[PubMed](#)]
5. Tang, Z.G.; Uchida, S.; Bessho, T.; Kinoshita, T.; Wang, H.B.; Awai, F.; Jono, R.; Maitani, M.M.; Nakazaki, J.; Kubo, T.; et al. Modulations of various alkali metal cations on organometal halide perovskites and their influence on photovoltaic performance. *Nano Energy* **2018**, *45*, 184–192. [[CrossRef](#)]
6. Stranks, S.D.; Eperon, G.E.; Grancini, G.; Menelaou, C.; Alcocer, M.J.P.; Leijtens, T.; Herz, L.M.; Petrozza, A.; Snaith, H.J. Electron-Solvent-vapor-pore Diffusion Lengths Exceeding 1 Micrometer in an Organometal Trihalide Perovskite Absorber. *Science* **2013**, *342*, 341–344. [[CrossRef](#)] [[PubMed](#)]
7. Eperon, G.E.; Burlakov, V.M.; Docampo, P.; Goriely, A.; Snaith, H.J. Morphological Control for High Performance, Solution-Processed Planar Heterojunction Perovskite Solar Cells. *Adv. Funct. Mater.* **2014**, *24*, 151–157. [[CrossRef](#)]
8. Chen, Z.; Li, H.; Tang, Y.; Huang, X.; Ho, D.; Lee, C.-S. Shape-Controlled Synthesis of Organolead Halide Perovskite Nanocrystals and Their Tunable Optical Absorption. *Mater. Res. Express* **2014**, *1*, 015034. [[CrossRef](#)]
9. Yin, W.J.; Shi, T.; Yan, Y. Unique Properties of Halide Perovskites as Possible Origins of the Superior Solar Cell Performance. *Adv. Mater.* **2014**, *26*, 4653–4658. [[CrossRef](#)] [[PubMed](#)]
10. Brenner, T.M.; Egger, D.A.; Kronik, L.; Hodes, G.; Cahen, D. Hybrid organic–inorganic perovskites: Low-cost semiconductors with intriguing charge-transport properties. *Nat. Rev. Mater.* **2016**, *1*, 15007. [[CrossRef](#)]
11. Bai, X.; Zou, X.; Zhu, J.; Pei, Y.; Yang, Y.; Jin, W.; Chen, D. Effect of Rb doping on modulating grain shape and semiconductor properties of $MAPbI_3$ perovskite layer. *Mater. Lett.* **2018**, *211*, 328–330. [[CrossRef](#)]

12. Yang, Y.; Zou, X.; Pei, Y.; Bai, X.; Jin, W.; Chen, D. Effect of doping of NaI monovalent cation halide on the structural, morphological, optical and optoelectronic properties of MAPbI₃ perovskite. *J. Mater. Sci. Mater. Electron.* **2018**, *29*, 205–210. [[CrossRef](#)]
13. Zhu, F.; Zhang, P.; Wu, X.; Fu, L.; Zhang, J.; Xu, D. The origin of higher open-circuit voltage in Zn-doped TiO₂ nanoparticle-based dye-sensitized solar cells. *ChemPhysChem* **2012**, *13*, 3731. [[CrossRef](#)] [[PubMed](#)]
14. Gao, Y.; Yip, H.L.; Chen, K.S.; O'malley, K.M.; Acton, O.; Sun, Y.; Ting, G.; Chen, H.; Jen, A.K.Y. Surface Doping of Conjugated Polymers by Graphene Oxide and Its Application for Organic Electronic Devices. *Adv. Mater.* **2011**, *23*, 1903. [[CrossRef](#)] [[PubMed](#)]
15. Li, Z.; Yang, M.; Park, J.S.; Wei, S.H.; Berry, J.J.; Zhu, K. Stabilizing Perovskite Structures by Tuning Tolerance Factor: Formation of Formamidinium and Cesium Lead Iodide Solid-State Alloys. *Chem. Mater.* **2016**, *28*, 284–292. [[CrossRef](#)]
16. Saliba, M.; Matsui, T.; Seo, J.-Y.; Domanski, K.; Correa-Baena, J.-P.; Nazeeruddin, M.K.; Zakeeruddin, S.M.; Tress, W.; Abate, A.; Hagfeldt, A.; et al. Cesium-containing triple cation perovskite solar cells: Improved stability, reproducibility and high efficiency. *Energy Environ. Sci.* **2016**, *9*, 1989–1997. [[CrossRef](#)] [[PubMed](#)]
17. Syzgantseva, O.A.; Saliba, M.; Grätzel, M.; Rothlisberger, U. Stabilization of the Perovskite Phase of Formamidinium Lead Triiodide by Methylammonium, Cs, and/or Rb Doping. *J. Phys. Chem. Lett.* **2017**, *8*, 1191–1196. [[CrossRef](#)] [[PubMed](#)]
18. Nam, J.K.; Chai, S.U.; Cha, W.; Choi, Y.J.; Kim, W.; Jung, M.S.; Kwon, J.; Kim, D.; Park, J.H. Potassium Incorporation for Enhanced Performance and Stability of Fully Inorganic Cesium Lead Halide Perovskite Solar Cells. *Nano Lett.* **2017**, *17*, 2028–2033. [[CrossRef](#)] [[PubMed](#)]
19. Chang, J.; Lin, Z.; Zhu, H.; Isikgor, F.H.; Xu, Q.-H.; Zhang, C.; Hao, Y.; Ouyang, J. Enhancing the photovoltaic performance of planar heterojunction perovskite solar cells by doping the perovskite layer with alkali metal ions. *J. Mater. Chem. A* **2016**, *4*, 16546–16552. [[CrossRef](#)]
20. Zhao, P.; Yin, W.; Kim, M.; Han, M.; Song, J. Improved carriers injection capacity in perovskite solar cells by introducing A-site interstitial defects. *J. Mater. Chem. A* **2017**, *5*, 7905–7911. [[CrossRef](#)]
21. Bag, S.; Durstock, M.F. Large Perovskite Grain Growth in Low-Temperature Solution-Processed Planar p-i-n Solar Cells by Sodium Addition. *ACS Appl. Mater. Interfaces* **2016**, *8*, 5053–5057. [[CrossRef](#)] [[PubMed](#)]
22. Bi, C.; Zheng, X.; Chen, B.; Wei, H.; Huang, J. Spontaneous Passivation of Hybrid Perovskite by Sodium Ions from Glass Substrates: Mysterious Enhancement of Device Efficiency Revealed. *ACS Energy Lett.* **2017**, *2*, 1400–1406. [[CrossRef](#)]
23. Tang, Z.G.; Bessho, T.; Awai, F.; Kinoshita, T.; Maitani, M.M.; Jono, R.; Murakami, T.N.; Wang, H.B.; Kubo, T.; Uchida, S.; et al. Hysteresis-free perovskite solar cells made of potassium-doped organometal halide perovskite. *Sci. Rep.* **2017**, *7*, 12183. [[CrossRef](#)] [[PubMed](#)]
24. Yao, D.S.; Zhang, C.M.; Pham, N.D.; Zhang, Y.H.; Tiong, V.T.; Du, A.J.; Shen, Q.; Wilson, G.J.; Wang, H.X. Hindered Formation of Photo-Inactive δ -FAPbI₃ Phase and Hysteresis-Free Mixed-Cation Planar Heterojunction Perovskite Solar Cells with Enhanced Efficiency via Potassium Incorporation. *J. Phys. Chem. Lett.* **2018**, *9*, 2113–2120. [[CrossRef](#)] [[PubMed](#)]
25. Kubicki, D.J.; Prochowicz, D.; Hofstetter, A.; Zakeeruddin, S.M.; Gratzel, M.; Emsley, L. Phase Segregation in Potassium-Doped Lead Halide Perovskites from K-39 Solid-State NMR at 21.1 T. *J. Am. Chem. Soc.* **2018**, *140*, 7232–7238. [[CrossRef](#)] [[PubMed](#)]
26. Abdi-Jalebi, M.; Andaji-Garmaroudi, Z.; Cacovich, S.; Stavrakas, C.; Philippe, B.; Richter, J.M.; Alsari, M.; Booker, E.P.; Hutter, E.M.; Pearson, A.J.; et al. Maximizing and stabilizing luminescence from halide perovskites with potassium passivation. *Nature* **2018**, *555*, 497–501. [[CrossRef](#)] [[PubMed](#)]
27. Kubicki, D.J.; Prochowicz, D.; Hofstetter, A.; Zakeeruddin, S.M.; Gratzel, M.; Emsley, L. Phase Segregation in Cs-, Rb- and K-Doped Mixed-Cation (MA)_x(FA)_{1-x}PbI₃ Hybrid Perovskites from Solid-State NMR. *J. Am. Chem. Soc.* **2017**, *139*, 14173–14180. [[CrossRef](#)] [[PubMed](#)]
28. Kojima, A.; Teshima, K.; Shirai, Y.; Miyasaka, T. Organometal halide perovskites as visible-light sensitizers for photovoltaic cells. *J. Am. Chem. Soc.* **2009**, *131*, 6050–6051. [[CrossRef](#)] [[PubMed](#)]
29. Yang, W.S.; Park, B.-W.; Jung, E.H.; Jeon, N.J.; Kim, Y.C.; Lee, D.U.; Shin, S.S.; Seo, J.; Kim, E.K.; Noh, J.H.; et al. Iodide management in formamidinium-lead-halide-based perovskite layers for efficient solar cells. *Science* **2017**, *356*, 1376–1379. [[CrossRef](#)] [[PubMed](#)]

30. Mei, A.; Li, X.; Liu, L.; Ku, Z.; Liu, T.; Rong, Y.G.; Xu, M.; Hu, M.; Chen, J.; Yang, Y.; et al. A hole-conductor-free, fully printable mesoscopic perovskite solar cell with high stability. *Science* **2014**, *345*, 295–298. [[CrossRef](#)] [[PubMed](#)]
31. Habisreutinger, S.N.; Leijtens, T.; Eperon, G.E.; Stranks, S.D.; Nicholas, R.J.; Snaith, H.J. Carbon nanotube/polymer composites as a highly stable hole collection layer in perovskite solar cells. *Nano Lett.* **2014**, *14*, 5561–5568. [[CrossRef](#)] [[PubMed](#)]
32. Wei, Z.; Yan, K.; Chen, H.; Yi, Y.; Zhang, T.; Long, X.; Li, J.; Zhang, L.; Wang, J.; Yang, S. Cost-efficient clamping solar cells using candle soot for hole extraction from ambipolar perovskites. *Energy Environ. Sci.* **2014**, *7*, 3326–3333. [[CrossRef](#)]
33. Zhang, N.; Guo, Y.; Yin, X.; He, M.; Zou, X. Spongy carbon film deposited on a separated substrate as counter electrode for perovskite-based solar cell. *Mater. Lett.* **2016**, *182*, 248–252. [[CrossRef](#)]
34. Ling, T.; Zou, X.; Cheng, J.; Bai, X.; Ren, H.; Chen, D. Modified Sequential Deposition Route through Localized-Liquid-Liquid-Diffusion for Improved Perovskite Multi-Crystalline Thin Films with Micrometer-Scaled Grains for Solar Cells. *Nanomaterials* **2018**, *8*, 416. [[CrossRef](#)] [[PubMed](#)]
35. Uz Zaman, M.M.; Imran, M.; Saleem, A.; Kamboh, A.H.; Arshad, M.; Khan, N.A.; Akhter, P. Potassium doped methylammonium lead iodide (MAPbI₃) thin films as a potential absorber for perovskite solar cells; structural, morphological, electronic and optoelectric properties. *Phys. B Condens. Matter* **2017**, *522*, 57–65. [[CrossRef](#)]
36. Luo, D.; Yu, L.; Wang, H.; Zou, T.; Luo, L.; Liu, Z.; Lu, Z. Cubic structure of the mixed halide perovskite CH₃NH₃PbI_{3-x}Cl_x via thermal annealing. *RSC Adv.* **2015**, *5*, 85480–85485. [[CrossRef](#)]
37. Li, C.; Guerrero, A.; Zhong, Y.; Graser, A.; Luna, C.A.M.; Kohler, J.; Bisquert, J.; Hildner, R.; Huettnner, S. Real-Time Observation of Iodide Ion Migration in Methylammonium Lead Halide Perovskites. *Small* **2017**, *13*, 1701711. [[CrossRef](#)] [[PubMed](#)]
38. Sun, Q.; Gong, X.; Li, H.; Liu, S.; Zhao, X.; Shen, Y.; Wang, M. Direct formation of I₃⁻ ions in organic cation solution for efficient perovskite solar cells. *Sol. Energy Mater. Sol. Cells* **2018**, *185*, 111–116. [[CrossRef](#)]



© 2018 by the authors. Licensee MDPI, Basel, Switzerland. This article is an open access article distributed under the terms and conditions of the Creative Commons Attribution (CC BY) license (<http://creativecommons.org/licenses/by/4.0/>).